

Chiral 1D Hybrid Metal Halides with Piezoelectric Energy Harvesting and Sensing Properties

Lian-Cai An, Chen Zhao, Ying Zhao, Ying Zhang, Kai Li, Alessandro Stroppa, Wei Li,* and Xian-He Bu*

Chiral hybrid metal halides have been widely studied in the field of photodetectors, chiral optics, and spintronics due to their great structural flexibility and suitable bandgaps. Inspired by such great progress made in the abovementioned fields, continuous efforts need to be paid to seek other interesting applications for chiral hybrid metal halides. Herein, the synthesis of a pair of one-dimensional enantiomorphic hybrid metal halide piezoelectrics, R/SMPcCl₄(R/SMP = R/S-2-methylpiperazine), and their applications in piezoelectric energy harvesting and sensing are reported. Density functional theory calculations show that these chiral piezoelectrics possess low elastic properties and high piezoelectric constants (16.71, 8.39, and 7.35 pC N⁻¹). In addition, devices made of RMPcCl₄/PDMS (PDMS = polydimethylsiloxane) composite films are fabricated for piezoelectric energy harvesting and sensing. The piezoelectric energy harvesters with optimized content of 15 wt% RMPcCl₄/PDMS show not only excellent performance with an open-circuit voltage of 2.57 V, short-circuit current of 0.37 μA, and power density of 0.55 μW cm⁻² but also outstanding stability of more than 3500 cycles. Meanwhile, these piezoelectric energy harvesters exhibit prominent sensing properties for detecting tapping, finger bending, walking, and running. It is demonstrated that chiral hybrid metal halides hold great potential in intelligent wearable and sensing devices.

1. Introduction

Piezoelectrics, an important class of material, which can convert mechanical energy to electric energy have been widely used as actuators, transducers, and sensors.^[1–6] The traditional commercial piezoelectrics including inorganic oxides (lead zirconate titanate, sodium potassium niobate, and zinc oxide) and organic polymers (polyvinylidene difluoride, PVDF) have been widely used in device applications.^[7–11] Inorganic oxides have excellent output performance under uploading forces but high stiffness while organic polymers usually have great softness but a limited output performance. However, new venues in smart wearable devices (such as electronic skins, self-powered pacemakers, and soft robots) require a combination of high piezoelectric performance and mechanical softness.^[12,13]


Organic–inorganic hybrid metal halides, consisting in inorganic polyhedral which endow them with excellent dielectric properties and organic cations which facilitate structural flexibility and low elastic

properties, have offered a new platform to search for piezoelectrics that meet needs.^[14–17] Currently, a series of significant progresses in hybrid organic–inorganic piezoelectrics have been succeeded.^[18–21] Especially, (TMFM)_{0.26}(TMCM)_{0.74}CdCl₃ (TMFM = trimethylfluoromethyl ammonium; TMCM = trimethylchloromethyl ammonium) optimized via morphotropic phase boundaries effect shows the piezoelectric coefficient d_{33} of 1540 pC N⁻¹ comparable to d_{33} of commercial oxides,^[22] and an extremely high g_{33} of 660.3×10^{-3} V m N⁻¹ was realized in (ATHP)₂PbBr₄ (ATHP = 4-aminotetrahydropyran).^[23] Apart from the single-component hybrid organic–inorganic piezoelectrics, considerable efforts have paid to their piezoelectric composite films with polymers (PDMS = polydimethylsiloxane, PVDF, TPU = thermoplastic polyurethanes) in order to better meet the acquires of practical applications.^[24–30] Very recently, a composite film composed of a ferroelectric crystal [(CH₃)₃NCH₂Cl][GaCl₄] and PDMS shows excellent piezoelectric properties of an open-circuit voltage of 38.1 V and a short-circuit current of 1.6 μA.^[31] Our group has reported the first chiral two-dimensional lead halide perovskites piezoelectrics, R-/S-[BPEA]₂PbI₄ (BPEA = 1-(4-bromophenyl) ethylammonium) with the multifunctionality of circularly polarized photoluminescence and piezoelectricity.^[32] Such chiral

L.-C. An, C. Zhao, Y. Zhao, Y. Zhang, W. Li, X.-H. Bu
School of Materials Science and Engineering
Smart Sensing Interdisciplinary Science Center
Nankai University & TKL of Metal and Molecule Based Material Chemistry
Tianjin 300350, China
E-mail: wl276@nankai.edu.cn; buxh@nankai.edu.cn

K. Li
Department of Chemistry and Chemical Engineering
Jinzhou University
Jinzhou, Shanxi 030619, China

A. Stroppa
CNR-SPIN c/o Department of Physical and Chemical Sciences
University of L'Aquila
Coppito, L'Aquila 67100, Italy

 The ORCID identification number(s) for the author(s) of this article can be found under <https://doi.org/10.1002/ssstr.202300135>.

© 2023 The Authors. Small Structures published by Wiley-VCH GmbH. This is an open access article under the terms of the Creative Commons Attribution License, which permits use, distribution and reproduction in any medium, provided the original work is properly cited.

DOI: 10.1002/ssstr.202300135

structures arising from the organic cations can not only show intrinsic piezoelectricity but also provide other chiral properties.

In this work, we report the structures, elastic properties, and piezoelectricity of chiral hybrid metal halides, R/SMPCdCl₄ (R/SMP = R-/S-2-methylpiperazine), via the experimental methods and first-principles calculations. Meanwhile, R/SMPCdCl₄/PDMS composite films with different contents were fabricated and explored their applications in piezoelectric energy harvesting and human motion sensing.

2. Results and Discussion

2.1. Crystal Structures of R/SMPCdCl₄

Crystals of R/SMPCdCl₄ both crystalize in an orthorhombic system, a chiral space group $P2_12_12_1$. The cell parameters of R/SMPCdCl₄ are $a = 5.83/5.85$, $b = 13.24/13.35$, and $c = 15.32/15.38$ Å, respectively. As shown in Figure 1a,c, both R/SMPCdCl₄ exhibit a typical one-dimensional packing structure in which [CdCl₄]_n²⁻ chains are propagating along *a* crystal axis. Due to the induction of enantiomers, the crystal structures of R/SMPCdCl₄ show a mirror-imaged relationship. In detail, each Cd²⁺ is coordinated with six Cl⁻ anions to form a [CdCl₆]⁴⁻ octahedron and further these octahedrons are linked with each other via two line-sharing connections to construct a wavy one-dimensional chain, [CdCl₄]_n²⁻ as shown in Figure S1, Supporting Information. These organic anions are located around the inorganic chains via electrostatic force and

N–H...Cl hydrogen bonds (2.18–2.26 Å) to further connect these chains. As for RacMPCd₂Cl₆·H₂O in Figure S2, Supporting Information, it crystallizes in a monoclinic system, a centrosymmetric space group $P2_1/n$ with the cell parameters $a = 12.13$, $b = 6.77$, $c = 18.50$ Å, $\beta = 94.09^\circ$. The octahedrons are linked via three line-sharing connections to build the inorganic chains.

To analyze and visualize the intermolecular interactions between the organic cations and the inorganic octahedrons, the Hirshfeld surfaces and corresponding 2D fingerprints were calculated and plotted.^[33–35] The different surface colors of red, white, and blue represent the different van der Waals distances which are shorter, equal to, and longer, respectively. As shown in the insert of Figure 1b,d, the Hirshfeld surfaces of R/SMP²⁺ both showed bright red areas in the –NH₂ groups suggesting the strong intermolecular interactions between the organic cations and inorganic chains. As for the 2D fingerprints, the d_i and d_e represent the distances between the organic cation and the surrounding atoms inside and outside of the Hirshfeld surface, respectively. One striking feature for both crystals is that the 2D fingerprints show a sharp peak (d_i , d_e) in the bottom left with (0.76, 1.35) and (0.77, 1.36) for R/SMPCdCl₄, respectively. From these peaks of the 2D fingerprints ($d_i < d_e$), it can be found that organic cations play the role of the strong hydrogen bond donor. Further, the sum ($d_i + d_e$) is relatively small suggesting the strong hydrogen bond between the chains and the organic cations. Powder X-ray diffractions (PXRD) of RMPCdCl₄ were conducted as shown in Figure S3a, Supporting Information, and the experimental pattern is well matched with the simulated

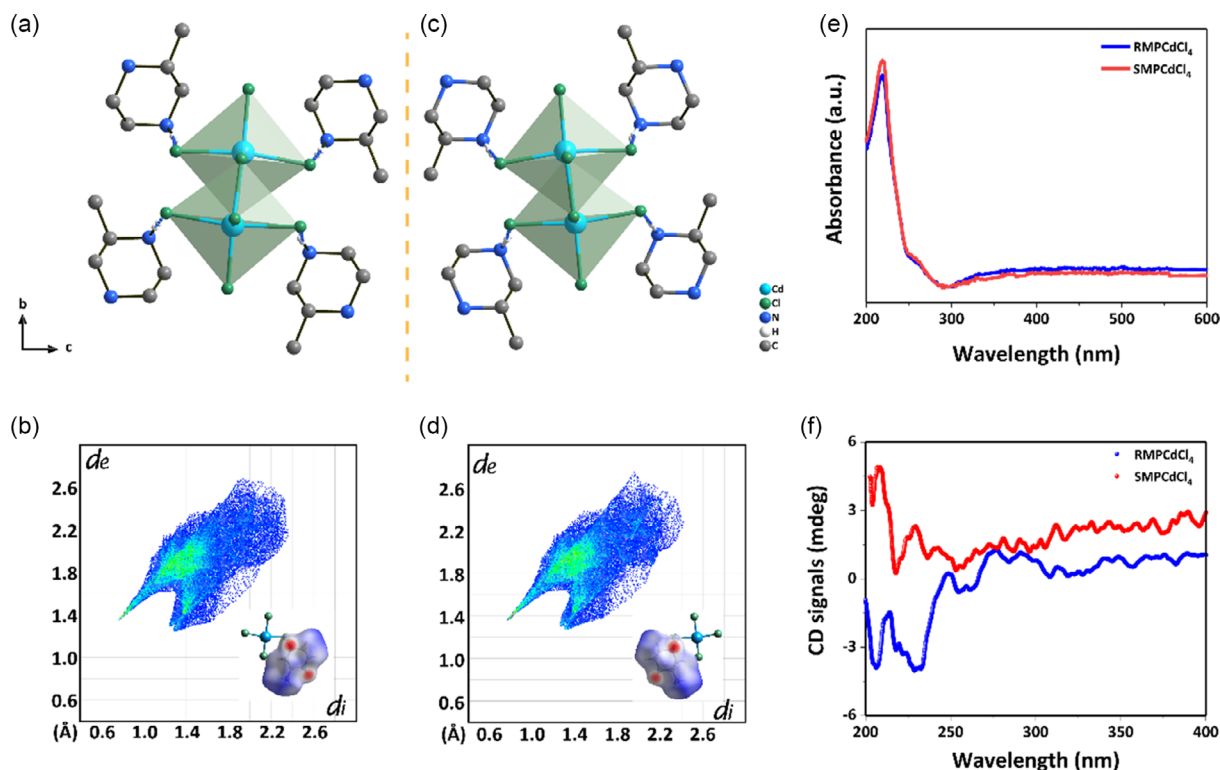


Figure 1. Crystal structures of a) RMPCdCl₄ and c) SMPCdCl₄ along the *a*-axis. Note that the extra hydrogen atoms except these of N–H...Cl hydrogen bonds are omitted for clarity. The 2D fingerprints of b) RMPCdCl₄ and d) SMPCdCl₄. The inserts are the Hirshfeld surfaces of the organic cations. e) UV-visible absorptions and f) CD signals of R/SMPCdCl₄.

one to verify the crystal powder purity. Further thermogravimetric (TG) (Figure S3b, Supporting Information) experiments of RMPCdCl_4 show that the compound does not decompose until 245 °C. Both Raman and infra-red spectroscopy (Figure S4, Supporting Information) are identical, which indicates their enantiomeric crystal structures.

Further, UV-visible absorptions of two crystals were measured at room temperature. The UV-visible absorptions of crystal powder were measured at room temperature to investigate the optical bandgaps. As shown in Figure 1e, both crystals show a clear absorption edge starting at around 250 nm. Then the optical bandgaps of crystals are determined as 4.96 eV. To verify the chirality of these enantiomers, circular dichroism (CD) spectroscopy was recorded using drop-casted thin films in the range of 200–400 nm as shown in Figure 1f. Due to the Cotton effect, R/SMPCdCl_4 films show typical chiral nature in which the opposite CD signals are observed at the same wavelength (typically at 215 nm). This result indicates that the chirality of the organic cations is transferred to the coordination chains which is widely reported in previous chiral hybrids.

2.2. Elastic Properties of R/SMPCdCl_4

The elastic properties are of great significance for chiral piezoelectrics since they can not only reflect the mechanical properties when the devices are working but also determine the intrinsic

piezoelectric performance. The elastic stiffness constants (C_{ij}) are first obtained through first-principles calculations^[36] and listed in Table S2 and S3, Supporting Information, and showing almost identical values for the R/SMPCdCl_4 . Based on C_{ij} , shear modulus (G), and Young's modulus (E) are depicted in Figure 2 and S5, Supporting Information, and the maximum and minimum values of various moduli and the corresponding directions are extracted and listed in Tables S4 and S5, Supporting Information. Taking an example of G of RMPCdCl_4 , the three-dimensional representation shows that the G_{max} is 11.81 GPa along (001) $\langle 010 \rangle$ direction and the G_{min} is 12.20 GPa along $(-110) \langle 110 \rangle$ direction. It could be easily rationalized from the crystal packing in Figure S6, Supporting Information. In the (001) $\langle 010 \rangle$ direction, the inorganic chains are linked via two line-sharing connections resulting in a more stable structure and fewer shear strains along this direction in Figure S6a, Supporting Information. On the contrary, the inorganic chains are more flexible and thus resulting in greater shear strains along $(-110) \langle 110 \rangle$ direction in Figure S6b, Supporting Information. Meanwhile, the anisotropy of G ($G_{\text{max}}/G_{\text{min}}$) is 2.40, which is much smaller than those of many reported hybrid materials.^[22,37,38] Young's moduli also show smaller values and anisotropies compared with the typical perovskite oxides.

Based on the elastic constant, we further obtained the piezoelectric constants of R/SMPCdCl_4 . Like the typical piezoelectric crystal, Rochelle salt,^[39,40] R/SMPCdCl_4 belongs to the

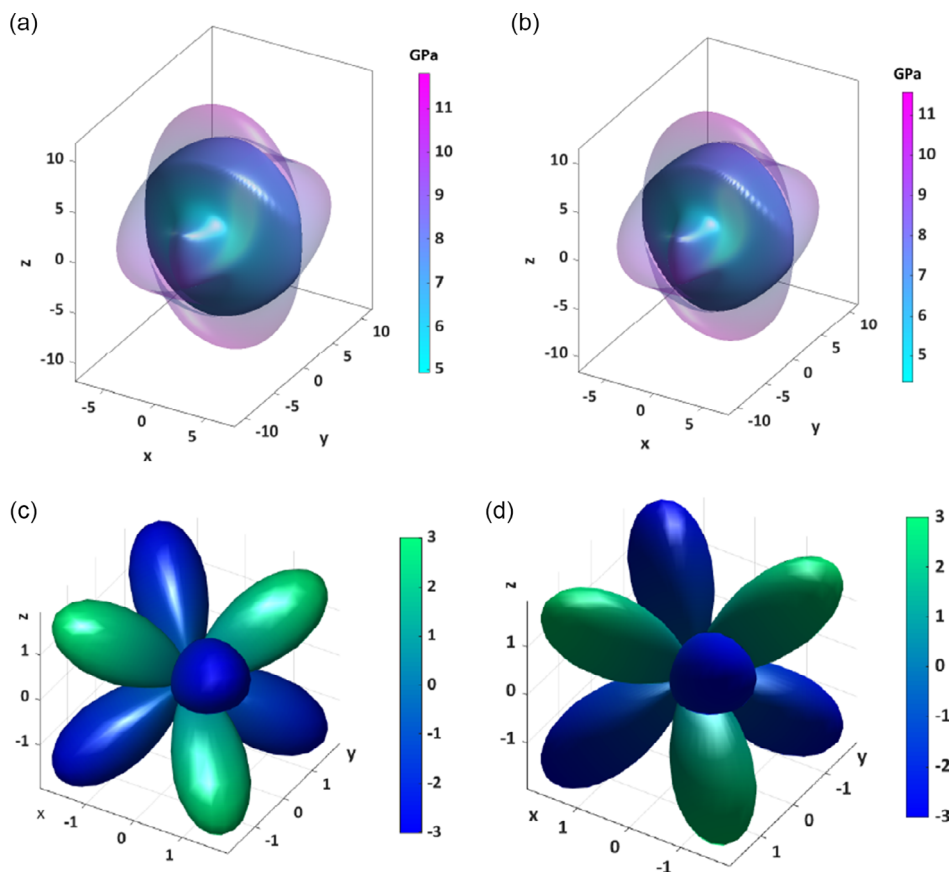


Figure 2. The elastic properties of R/SMPCdCl_4 . The 3D representations of a,b) shear moduli and c,d) piezoelectric constants of R/SMPCdCl_4 .

orthorhombic 222-point group and has shear piezoelectric constants, d_{14} , d_{25} , and d_{36} . To obtain the piezoelectric strain tensor $[d]$, we calculated the equation of $[d] = [e][s]$, where e and s denote piezoelectric stress constants and elastic compliance constants obtained from theoretical calculations, respectively. The 3D and 2D representations of d are shown in Figure 2c,d, S7, Supporting Information, and the d_{ij} are listed in Table S6, Supporting Information. As for RMPCdCl₄, values of d_{14} , d_{25} , and d_{36} are 16.71, 8.39, and 7.35 pC N⁻¹, respectively. Such values are comparable with those of crystal materials.^[18,41,42] From the above-mentioned equation of piezoelectric constants, it can be concluded that to improve the natural piezoelectricity is to increase the polarization and decrease the crystal stiffness. So, these high shear piezoelectric constants might be attributed to the small elastic stiffness constants and the overall low Young's and shear moduli.

2.3. Characterizations of RMPCdCl₄/PDMS Composite Films

Considering the soft nature and the good piezoelectric activity, R/SMPCdCl₄ might be a potential candidate for the flexible wearing self-power device. To investigate the piezoelectric energy harvesting and sensing properties and optimize the components, a series of composite films of RMPCdCl₄/PDMS with a weight

ratio (wt%) of crystal powder from 5, 10, 15, to 20 wt% were prepared. As shown in Figure 3a, the homogeneous white composite films of 15 wt% with 2 × 2 cm² can be easily folded with tweezers and display good flexibility for practical applications. Moreover, PXRD patterns of different content films (Figure 3b and S8, Supporting Information) show that the structure of the crystal is well preserved with the remaining peaks at 8.82°/(011) face, 20.26°/(112) face, and 21.10°/(121) face. As the content increase, the other diffraction peaks are also shown indicating the gradually improved crystallinity. In detail for 15 wt% content, the PXRD pattern is well matched with the simulated pattern indicating that all the crystal particles are randomly and evenly distributed in the composite film. Furthermore, the SEM image of 15 wt% content film (Figure 3c) shows the uniform morphology of the cross-section with a thickness of approximately 200 μm. The EDS mapping of Si, Cd, and Cl, clearly shows that the crystal particles are distributed evenly in the PDMS matrix. The uniform distribution of crystal particles is also found in the polarizing photos in Figure S9, Supporting Information. The lamellar crystals of RMPCdCl₄ are uniformly dispersed in the PDMS substrate. As the content of crystal particles increases, the size of crystal particles is also getting bigger as expected. The statistical particle dimeters are varied from 9.63 to 12.72 μm as the content of RMPCdCl₄ is increasing from 5 to 20 wt%. Such particle aggregation effect is also seen in the

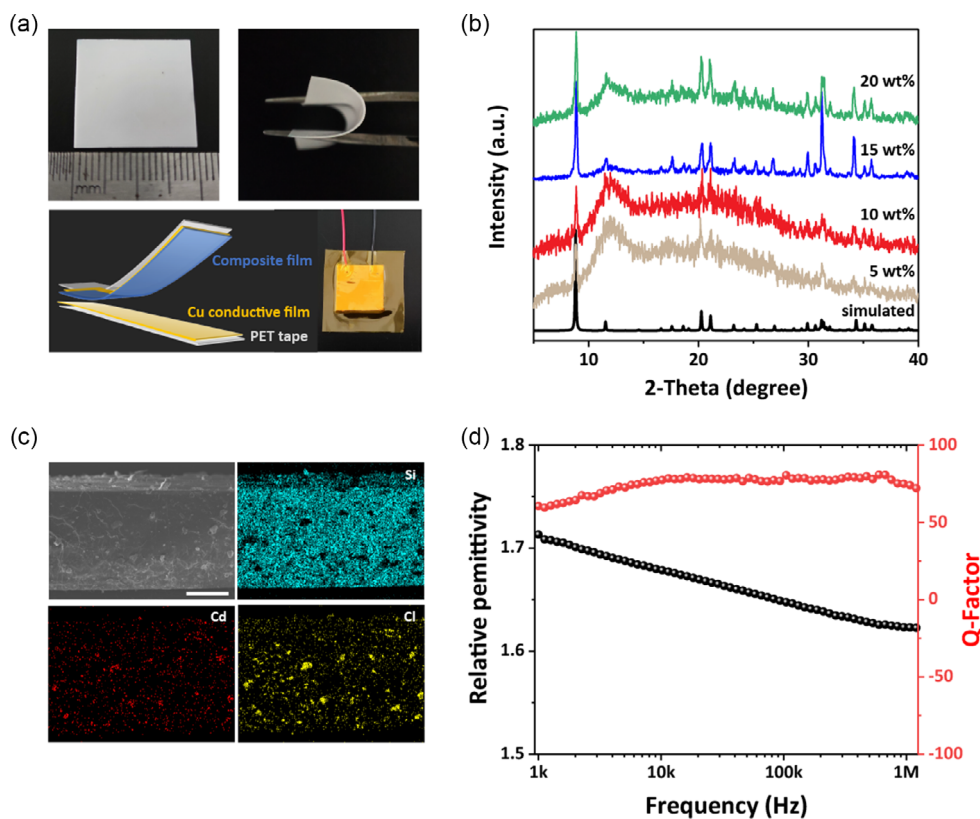


Figure 3. The phase characteristics of the as-prepared RMPCdCl₄/PDMS films. a) The optical image of the original composite film and the folded films with tweezers (top). The schematic representation of the piezoelectric device with a sandwich structure and the real device for the later experiments (bottom). b) The PXRD patterns of the RMPCdCl₄/PDMS films with different contents. c) The cross-sectional SEM and EDS mapping images of 15 wt% RMPCdCl₄/PDMS composite films. Note that the insert bar in SEM represents 100 μm. d) The relative permittivity and quality factor of 15 wt% RMPCdCl₄ piezoelectric energy harvester.

SMPCdCl₄ films in Figure S9 and S10, Supporting Information. As shown in Figure S11, Supporting Information, 20 wt% RMPCdCl₄/PDMS films show larger grain sizes which could be attributed to the agglomeration of the piezoelectric particles.

The R/SMPCdCl₄/PDMS composite films are further utilized to fabricate the piezoelectric energy harvester with a sandwich structure as shown in Figure 3a. As for the practical piezoelectric applications, the dielectric property is one of the key factors. The relative permittivity (ϵ_r) and quality factor (Q) were collected to investigate the impedance properties of 15 wt% RMPCdCl₄ piezoelectric energy harvester (Figure 3d). Based on the frequency-dependent capacitance (Figure S12, Supporting Information), the relative permittivity is recorded and shows a slight fall as the frequency increases in the range of 1 k–1.2 MHz with a range from 1.62 to 1.71. Such lower relative permittivity of RMPCdCl₄ piezoelectric energy harvester compared with the pure compound (Figure S13, Supporting Information) and the traditional perovskite ceramics would promote the piezoelectric response according to the relation of $g = d/\epsilon_r$, where g is the piezoelectric voltage constant, ϵ_r is the relative permittivity, and d is the piezoelectric constant. Further, RMPCdCl₄ piezoelectric energy harvester shows a relatively small Q factor of 74.4, which might indicate the potential applications in sensors and detectors. The relative permittivity (ϵ_r) and quality factor (Q) of 15 wt% SMPCdCl₄ PEG are also obtained in Figure S14, Supporting Information. Furthermore, the impedances of RMPCdCl₄ crystals and composite films were compared in Figure S15, Supporting Information. The composite films show a smaller impedance than RMPCdCl₄, which suggests that the piezoelectric devices would produce a greater power density than RMPCdCl₄ pellets.

2.4. Piezoelectric Energy Harvesting and Human Motion Sensing

To investigate the piezoelectric performance of R/SMPCdCl₄, the as-prepared piezoelectric energy harvester is tested in a homemade piezoelectric test system with the periodic mechanical tapping of 10 Hz. Upon applying the pressing force of 2 N to the piezoelectric energy harvester, an electric dipole could be generated, resulting in piezoelectric charges flowing to the electrodes, and the open-circuit piezoelectric voltages (V_{oc}) of different content are shown in Figure 4a. As the content increases from 5 to 15 wt%, the values of V_{oc} are also increasing from 0.97, 1.17, to 2.57 V. The output performance of V_{oc} is more outstanding than that of chiral molecular crystals^[41] and chiral lead halide perovskites. It suggests that the piezoelectric outperformance of the composite films is positively dependent on the active piezoelectric component content among the relatively low content and the optimized content for the RMPCdCl₄ composite films is 15 wt%. Within the content range, the piezoelectric active components play a dominant role in improving the piezoelectric energy harvester performance. However, with the further increase of the content up to 20 wt%, the performance of V_{oc} conversely decreases to 0.91 V. Such deteriorated performance might arise from the excessive aggregation of active particles as shown in the SEM and polarizing images. The significant increase of the

particle size in the 20 wt% RMPCdCl₄/PDMS films inevitably results in enhanced dielectric constants and a Maxwell–Wagner–Sillars polarization so that the high content of the piezoelectric particle would deteriorate rather than improve the piezoelectric response. The same trend is observed in the short-circuit current (I_{sc}) in Figure 4d that the piezoelectric energy harvester of optimized 15 wt% content shows a better performance of 0.37 μ A. Based on the output performance of different contents, piezoelectric energy harvester with 15 wt% RMPCdCl₄ films is selected to conduct further piezoelectric tests.

To confirm the piezoelectric effect, the outputs of V_{oc} (Figure 4b) and I_{sc} (Figure 4e) were recorded when the electrodes were connected forward and reversed. Taking an example of Figure 4b, V_{oc} shows typically positive values when the electrodes were connected forward while it shows almost identical but negative values when the electrode was connected reversed. The flipping of outputs verifies these signals truly come from the piezoelectric effect rather than the triboelectric effect.^[26,30] Further the output signals were collected via applying different external forces from 1 to 5 N as shown in Figure 4c,f. With the increasing loading forces, the V_{oc} values reached from 2.23 to 3.55 V, and the I_{sc} values reached from 0.20 to 0.38 μ A showing a positive proportional trend. As for SMPCdCl₄ piezoelectric energy harvester, it also shows the same optimized content of 15 wt% with the output performance of 1.81 V in Figure S16a, Supporting Information. The electrode flipping test shows good reversibility for 5 wt% under the compressing force of 2 N in Figure S16b, Supporting Information. The output performance is also increasing up to 1.55 V with the increasing forces for 5 wt% piezoelectric energy harvesters in Figure S16c, Supporting Information. The output performance of the piezoelectric energy harvester was tested in dependence on frequency. As shown in Figure S17, Supporting Information, the output voltages increase with increasing frequency because the piezoelectric energy harvester can produce more charge per unit of time with increasing frequency. The potential utility of 15 wt% RMPCdCl₄/PDMS device was demonstrated by storing the harvested energy in 1 μ F capacitors (Figure S18, Supporting Information). As shown in the charging curve, the charges increase gradually and reach 0.35 μ C after 50 s.

To obtain the power density of RMPCdCl₄ piezoelectric energy harvester, the various voltages are collected with the different external load resistances in Figure 4g. With the external loading resistances increase, the output voltage is also gradually increased from 0.45 to 1.41 V. According to the power density (P) equation of $P = U^2/R$, where U is the output voltage and R is the external loading resistance, the different power densities were calculated in Figure 4g. The value of the power density reaches a maximum of 0.55 μ W cm⁻² at an external loading resistance of 2 M Ω which is comparable with that of pure PVDF films (Table S7, Supporting Information). Stability is another key parameter for practical applications. To check the mechanical and time stabilities of the 15 wt% RMPCdCl₄ piezoelectric energy harvester, the long-term output performance test is conducted under the continuous 2 N force at 10 Hz in Figure 4h. As the figure shows, piezoelectric energy harvester does not show any performance degradations throughout the 350 s testing, more than 3500 cycles. It suggests that RMPCdCl₄ piezoelectric

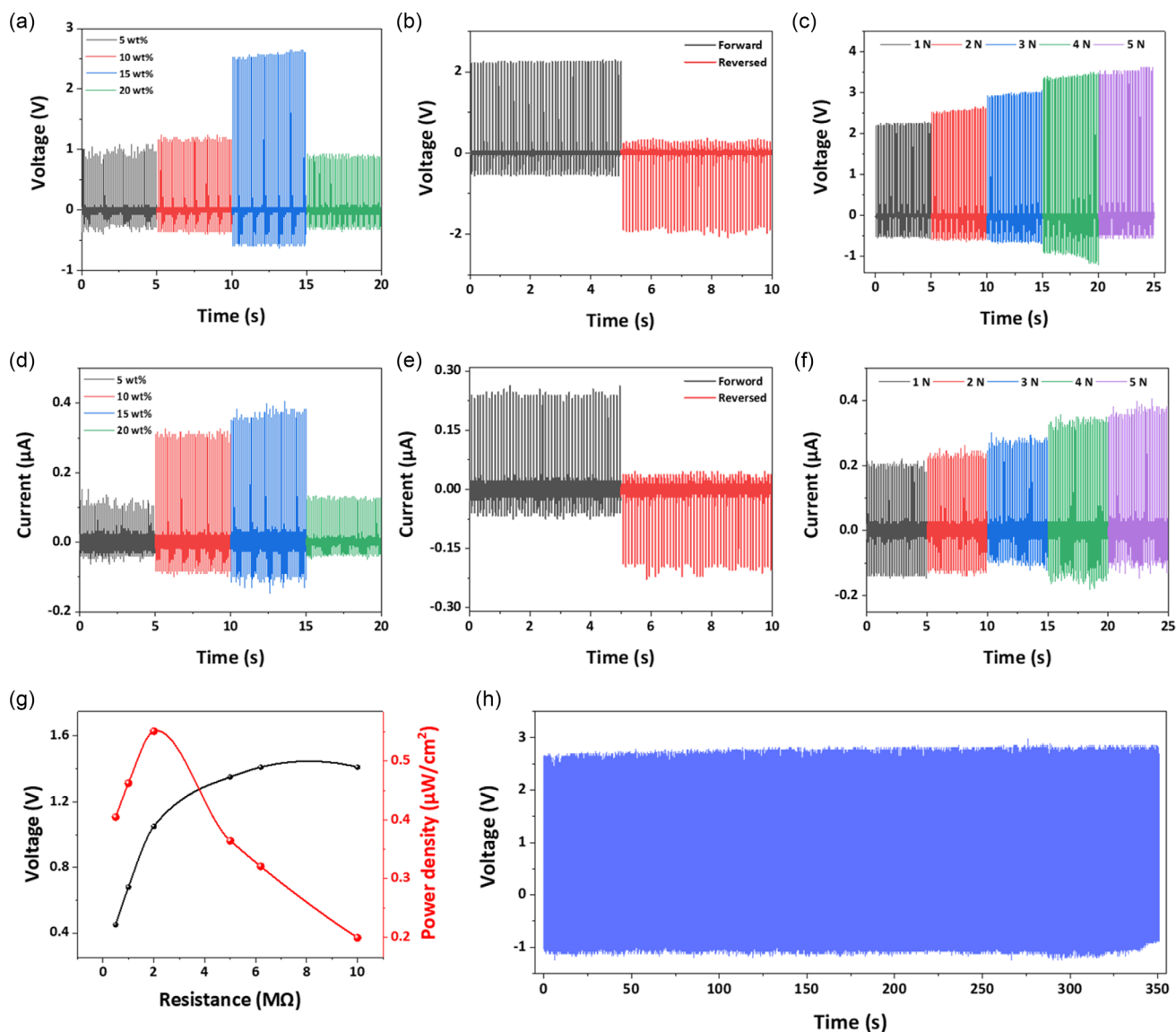


Figure 4. The piezoelectric output performance of RMPCdCl₄ piezoelectric energy harvesters. The piezoelectric energy harvester output performance of a) V_{oc} and d) I_{sc} with different contents of RMPCdCl₄. The piezoelectric energy harvester output performance of b) V_{oc} and e) I_{sc} . The output signals flipping test of b) V_{oc} and e) I_{sc} . The applying force-dependent c) V_{oc} and f) I_{sc} performances with 15 wt% RMPCdCl₄. g) The resistance-dependent voltages and power densities. h) The long-term output performance with 3500 cycles under 2 N force of 10 Hz.

energy harvester can guarantee stable output performance in working conditions.

Subsequently, 15 wt% RMPCdCl₄ piezoelectric energy harvester was utilized as the sensor to detect human motions (tapping, finger bending, walking, and running). As shown in Figure 5a, the slight tapping (approximately 0.1 N) can provoke the device to generate 0.5 V output with sharp peaks suggesting good sensitivity. Due to the excellent flexibility of RMPCdCl₄ piezoelectric energy harvester, the device was strapped to the knuckle to detect the finger bending and releasing as shown in Figure 5b. RMPCdCl₄ piezoelectric energy harvester produces a positive voltage (about 0.2 V) with the finger bending while when the bending is releasing, it generates an identical but

negative voltage. Because of the relatively slow motion compared with the tapping, the peaks of the finger bending and releasing are gentle and symmetrical. Furthermore, our piezoelectric energy harvester is equipped on the shoes to detect walking and running as shown in Figure 5c. The harvester can produce a positive voltage when the footstep falls while a relatively small negative voltage when the footstep is up. Compared to the voltages of gentle walking (1.3 V), running can produce a greater voltage (2.4 V). From the cycle numbers of output voltages, we can obtain the stride frequency per second of walking (1.2) and running (2.6). The abovementioned results imply that RMPCdCl₄ piezoelectric energy harvester has great potential in precise human motion sensors and other intelligent wearable devices.

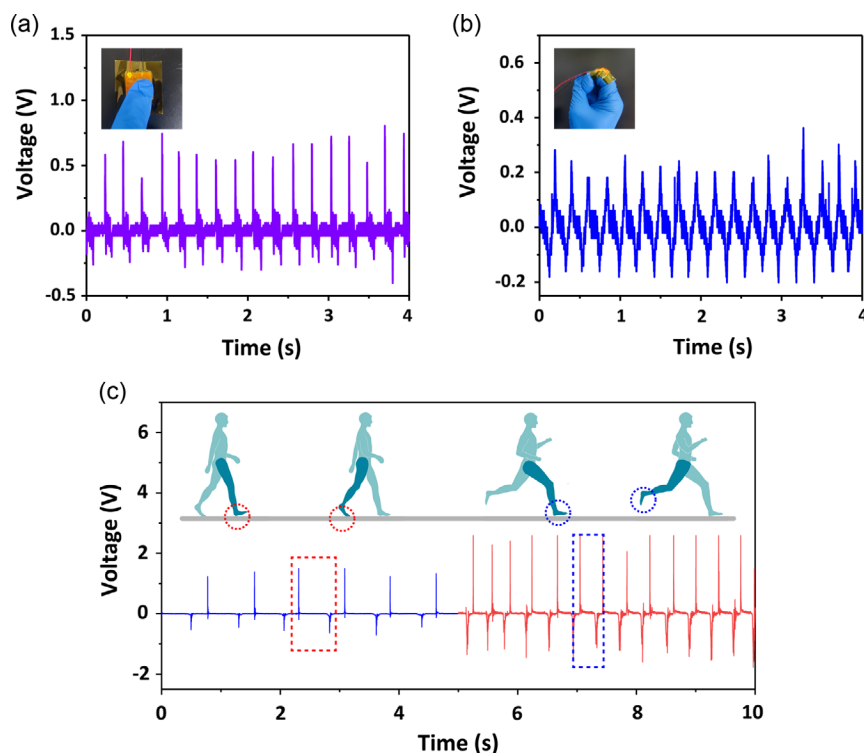


Figure 5. Human motion sensing tests. a) Tapping sensing and b) finger bending sensing of RMPCdCl₄ piezoelectric energy harvester. c) Human motion, walking, and running detection experiments.

3. Conclusion

In summary, two homochiral crystals, R/SMPCdCl₄, and the corresponding racemic crystal have been successfully synthesized by introducing the homochiral and racemic organic cations. Density functional theory (DFT) calculations show that R/SMPCdCl₄ would have low elastic moduli and attractive piezoelectricity which makes it suitable for piezoelectric applications. Furthermore, the optimized content, 15 wt% RMPCdCl₄/PDMS films are utilized in piezoelectric energy harvester and show attractive energy harvesting performance with maximum V_{oc} of 2.57 V, I_{sc} of 0.37 μ A, and power density of 0.55 μ W cm⁻² under an external force of 2 N. Meanwhile, the homochiral composite piezoelectric energy harvester exhibits great sensing property for detecting human sensing (tapping, finger bending, walking, and running) so it holds promise in intelligent wear devices. Our work develops the homochiral hybrid crystals and implies great potential applications in piezoelectric applications.

4. Experimental Section

Crystal Synthesis: All the chemicals and solvents used in this work were purchased from commercial vendors and used directly without further purification. Single crystals were synthesized via a similar method by mixing the stoichiometric amounts of CdCl₂ and the corresponding R-/S-/Rac- 2-methylpiperazine in HCl/H₂O solution (1 mL:1 mL) in a bottle. All the precipitates were dissolved by an ultrasonic oscillator to obtain a clear solution. After the solvent evaporation for two weeks, colorless transparent rod-shaped crystals were obtained in the bottom of a bottle.

Single Crystal Data Collection and Refinement: Single-crystal X-ray diffraction of R/SMPCdCl₄ was conducted on a Rigaku XtaLAB MM007 CCD diffractometer (Cu K α λ = 1.5418 Å). Structural solving using the ShelXT program and data refinement using the ShelXL Least Squares program were performed on the Olex2 software packages.^[43,44] All non-hydrogen atoms were refined anisotropically, whereas the hydrogen atoms were located and refined geometrically. The X-ray crystallographic structures of RMPCdCl₄, SMPCdCl₄, and RacMPCd₂Cl₆·H₂O have been deposited at the Cambridge Crystallographic Data Centre with the CCDC numbers of 2 208 000, 2 211 550, and 2 211 519, respectively. The crystal data and structure refinement parameters are summarized in Table S1, Supporting Information.

General Measurements: The circular dichroism (CD) spectra were acquired using a CD spectrometer (BioLogic, MOS-450). The solid-state ultraviolet-visible (UV-Vis) diffuse reflectance spectra were obtained on Thermo Fisher, Evolution 220. The SEM and EDS mapping were investigated by a field-emission scanning electron microscope, JSM-7800F. The powders and composite films X-ray diffractions were conducted on a Rigaku MiniFlex 600 diffractometer. The TG/DTA curves were obtained on a Rigaku standard TG-DTA analyzer from room temperature to 800 °C under an air atmosphere with a heating rate of 10 °C min⁻¹ using an empty and clean Al₂O₃ crucible as a reference. The impedance and conductivity were measured with a precision impedance analyzer (Wayne Kerr, 6500B). The polarizing photos were recorded on a Nikon LV100NPOL microscope.

R/SMPCdCl₄/PDMS Composite Film Preparations: 5, 10, 15, and 20 wt% (125, 250, 375, and 500 mg) well-grinded R/SMPCdCl₄ powders were added into 2.5 g PDMS precursor. Then 15 mL dichloromethane (CH₂Cl₂) was added into the precursor, and the mixture was stirred for 4 h to obtain a homogeneous solution. When CH₂Cl₂ was almost evaporating out, 10 wt% (250 mg) hardeners were added to the viscous liquid and stirred for pre-cure. The mixture was placed in a vacuum oven to remove the remaining CH₂Cl₂ and the bubbles in the precursor. Finally, the precursor was spread on the substrate to get a uniform

0.3 mm-thick film precursor and a piece of elastic film was obtained after post-cure for 1 h at 60 °C.

Piezoelectric Energy Harvester Fabrication and Test: The obtained films were cut into 2 cm × 2 cm squares and acting as the piezoelectric layers. The copper tapes were acting a role of a collector on both sides of the composite films. Finally, the entire device was encapsulated with PET tape for piezoelectric testing. The homemade piezoelectric output testing system was described in our previous work.^[45]

The capacitances, the impedances, and Q factors of composite films and the pure compound are obtained from a precision impedance analyzer (Wayne Kerr, 6500B). The relative permittivity is further obtained from the capacitances according to the equation: $\epsilon_r = Cd/\epsilon_0 \cdot S$, where C is the capacitances, d is the thickness, and S is the area.

The Statement for Human Subjects: The author who participated in the human motion sensing tests, has given informed signed consent.

Density Functional Theory (DFT) Calculations: The elastic and piezoelectric constants of crystals were obtained by the Vienna ab initio simulation package based on the DFT plane-wave pseudopotential method.^[46–48] The energy cutoff was set to 500 eV, and the k -point mesh spanning scheme of Monkhorst–Pack was $4 \times 2 \times 1$. Perdew–Burke–Ernzerh of generalized gradient approximation was used as the exchange–correlation energy function to optimize the atomic positions and lattice parameters until the total energy converged to within 10^{-7} eV and the residual forces on each atom were less than 0.01 eV \AA^{-1} .^[49] The elastic stiffness constants C_{ij} were obtained by the finite-strain method with 0.015 \AA of the maximum strain amplitude and 6 steps for each strain.^[50,51] The piezoelectric stress constants $[e]$ were calculated by using density functional perturbation theory, and then, the piezoelectric strain constants $[d]$ can be obtained by the following formula: $[d] = [e] * [s]$, where $[s]$ is the elastic compliance constants, equal to the inverse matrix of C_{ij} .^[52–54]

Supporting Information

Supporting Information is available from the Wiley Online Library or from the author.

Acknowledgements

This work was financially supported by the National Natural Science Foundation of China (Nos. 21975132, 22035003, and 21991143) and the Fundamental Research Funds for the Central Universities (No. 63196006). The corresponding authors have been updated on 10 July 2023, after initial online publication of the Version of Record.

Conflict of Interest

The authors declare no conflict of interest.

Data Availability Statement

The data that support the findings of this study are available from the corresponding author upon reasonable request.

Keywords

chiral hybrid metal halides, elastic properties, human motion sensing, piezoelectric constants, piezoelectric energy harvester

Received: April 13, 2023

Revised: June 4, 2023

Published online: June 27, 2023

- [1] K. Uchino, *Acta Mater.* **1998**, *46*, 3745.
- [2] S. Alkoy, J. F. Tressler, R. E. Newnham, *J. Electroceram.* **1998**, *2*, 257.
- [3] A. Petritz, E. Karner-Petritz, T. Uemura, P. Schäffner, T. Araki, B. Stadlober, T. Sekitani, *Nat. Commun.* **2021**, *12*, 2399.
- [4] F. Pop, B. Herrera, M. Rinaldi, *Nat. Commun.* **2022**, *13*, 1782.
- [5] X. Qing, W. Li, Y. Wang, H. Sun, *Sensors* **2019**, *19*, 545.
- [6] F. Yang, J. Li, Y. Long, Z. Zhang, L. Wang, J. Sui, Y. Dong, Y. Wang, R. Taylor, D. Ni, W. Cai, P. Wang, T. Hacker, X. Wang, *Science* **2021**, *373*, 337.
- [7] D. Damjanovic, *Rep. Prog. Phys.* **1998**, *61*, 1267.
- [8] H. Kawai, *Jpn. J. Appl. Phys.* **1969**, *8*, 975.
- [9] M. Kroutvar, Y. Ducommun, D. Heiss, M. Bichler, D. Schuh, G. Abstreiter, J. J. Finley, *Nature* **2004**, *432*, 81.
- [10] W. Liu, B. Jiang, W. Zhu, *Appl. Phys. Lett.* **2000**, *77*, 1047.
- [11] J. Rouquette, J. Haines, V. Bornand, M. Pintard, P. Papet, C. Bousquet, L. Konczewicz, F. A. Gorelli, S. Hull, *Phys. Rev. B* **2004**, *70*, 014108.
- [12] F. Ali, W. Raza, X. Li, H. Gul, K.-H. Kim, *Nano Energy* **2019**, *57*, 879.
- [13] Z. Yang, S. Zhou, J. Zu, D. Inman, *Joule* **2018**, *2*, 642.
- [14] K. Li, Z. G. Li, J. Xu, Y. Qin, W. Li, A. Stroppa, K. T. Butler, C. J. Howard, M. T. Dove, A. K. Cheetham, X. H. Bu, *J. Am. Chem. Soc.* **2022**, *144*, 816.
- [15] Y.-M. Liu, K. Li, T.-M. Guo, L.-C. An, Z.-Z. Zhang, M.-H. Yu, W. Li, X.-H. Bu, *ACS Mater. Lett.* **2022**, *4*, 1168.
- [16] L. P. Miao, N. Ding, N. Wang, C. Shi, H. Y. Ye, L. Li, Y. F. Yao, S. Dong, Y. Zhang, *Nat. Mater.* **2022**, *21*, 1158.
- [17] W. Li, Z. Wang, F. Deschler, S. Gao, R. H. Friend, A. K. Cheetham, *Nat. Rev. Mater.* **2017**, *2*, 16099.
- [18] Y. Hu, K. Parida, H. Zhang, X. Wang, Y. Li, X. Zhou, S. A. Morris, W. H. Liew, H. Wang, T. Li, F. Jiang, M. Yang, M. Alexe, Z. Du, C. L. Gan, K. Yao, B. Xu, P. S. Lee, H. J. Fan, *Nat. Commun.* **2022**, *13*, 5607.
- [19] W.-Q. Liao, Y.-Y. Tang, P.-F. Li, Y.-M. You, R.-G. Xiong, *J. Am. Chem. Soc.* **2017**, *139*, 18071.
- [20] H. Y. Zhang, Z. X. Zhang, X. J. Song, X. G. Chen, R. G. Xiong, *J. Am. Chem. Soc.* **2020**, *142*, 20208.
- [21] Y. Zhang, X.-J. Song, Z.-X. Zhang, D.-W. Fu, R.-G. Xiong, *Matter* **2020**, *2*, 697.
- [22] W.-Q. Liao, D. Zhao, Y.-Y. Tang, Y. Zhang, P.-F. Li, P.-P. Shi, X.-G. Chen, Y.-M. You, R.-G. Xiong, *Science* **2019**, *363*, 1206.
- [23] S. Deswal, S. K. Singh, P. Rambabu, P. Kulkarni, G. Vaitheeswaran, B. Praveenkumar, S. Ogale, R. Boomishankar, *Chem. Mater.* **2019**, *31*, 4545.
- [24] J. Dhar, S. Sil, N. A. Hoque, A. Dey, S. Das, P. P. Ray, D. Sanyal, *ChemistrySelect* **2018**, *3*, 5304.
- [25] R. Ding, X. Zhang, G. Chen, H. Wang, R. Kishor, J. Xiao, F. Gao, K. Zeng, X. Chen, X. W. Sun, Y. Zheng, *Nano Energy* **2017**, *37*, 126.
- [26] G. Huang, A. A. Khan, M. M. Rana, C. Xu, S. Xu, R. Saritas, S. Zhang, E. Abdel-Rahmand, P. Turban, S. Ababou-Girard, C. Wang, D. Ban, *ACS Energy Lett.* **2020**, *6*, 16.
- [27] Y.-J. Gong, Z.-G. Li, H. Chen, T.-M. Guo, F.-F. Gao, G.-J. Chen, Y. Zhang, Y.-M. You, W. Li, M. He, X.-H. Bu, J. Yu, *Matter* **2023**, *6*, 2066.
- [28] Y. Zhao, L.-C. An, K. Li, Y.-J. Gong, T.-M. Guo, F.-F. Gao, Y. Lei, Q. Li, W. Li, X.-H. Bu, *Sci. China Mater.* **2023**, *66*, 1854.
- [29] S. Ippili, V. Jella, J. Kim, S. Hong, S. G. Yoon, *ACS Appl. Mater. Interfaces* **2020**, *12*, 16469.
- [30] A. A. Khan, G. Huang, M. M. Rana, N. Mei, M. Biondi, S. Rassell, N. Tanguy, B. Sun, Z. Leonenko, N. Yan, C. Wang, S. Xu, D. Ban, *Nano Energy* **2021**, *86*, 106039.
- [31] B. Wang, J. Hong, Y. Yang, H. Zhao, L. Long, L. Zheng, *Matter* **2022**, *5*, 1296.

- [32] Y. Qin, F.-F. Gao, S. Qian, T.-M. Guo, Y.-J. Gong, Z.-G. Li, G. D. Su, Y. Gao, W. Li, C. Jiang, P. Lu, X.-H. Bu, *ACS Nano* **2022**, *16*, 3221.
- [33] D. J. Carter, P. Raiteri, K. R. Barnard, R. Gielink, M. Mocerino, B. W. Skelton, J. G. Vaughan, M. I. Ogden, A. L. Rohl, *CrystEngComm* **2017**, *19*, 2207.
- [34] J. J. McKinnon, M. A. Spackman, A. S. Mitchell, *Acta Crystallogr., Sect. B: Struct. Sci* **2004**, *60*, 627.
- [35] M. A. Spackman, J. J. McKinnon, *CrystEngComm* **2002**, *4*, 378.
- [36] K. Li, Y. Qin, Z.-G. Li, T.-M. Guo, L.-C. An, W. Li, N. Li, X.-H. Bu, *Coord. Chem. Rev.* **2022**, *470*, 214692.
- [37] L.-C. An, K. Li, Z.-G. Li, S. Zhu, Q. Li, Z.-Z. Zhang, L.-J. Ji, W. Li, X.-H. Bu, *Small* **2021**, *17*, 2006021.
- [38] J. H. Fan, Y. Qin, M. Azeem, Z. Z. Zhang, Z. G. Li, N. Sun, Z. Q. Yao, W. Li, *Dalton Trans.* **2021**, *50*, 2648.
- [39] C. Beevers, W. Hughes, *Nature* **1940**, *146*, 96.
- [40] R. E. Newnham, L. Eric Cross, *MRS Bull.* **2005**, *30*, 845.
- [41] W. Ji, B. Xue, Y. Yin, S. Guerin, Y. Wang, L. Zhang, Y. Cheng, L. J. W. Shimon, Y. Chen, D. Thompson, R. Yang, Y. Cao, W. Wang, K. Cai, E. Gazit, *J. Am. Chem. Soc.* **2022**, *144*, 18375.
- [42] H. S. Wu, S. M. Wei, S. W. Chen, H. C. Pan, W. P. Pan, S. M. Huang, M. L. Tsai, P. K. Yang, *Adv. Sci.* **2022**, *9*, 2105974.
- [43] O. V. Dolomanov, L. J. Bourhis, R. J. Gildea, J. A. K. Howard, H. Puschmann, *J. Appl. Crystallogr.* **2009**, *42*, 339.
- [44] G. Sheldrick, *Acta Crystallogr., Sect. B: Struct. Sci* **2015**, *71*, 3.
- [45] T.-M. Guo, Y.-J. Gong, Z.-G. Li, Y.-M. Liu, W. Li, Z.-Y. Li, X.-H. Bu, *Small* **2022**, *18*, 2103829.
- [46] G. Kresse, J. Furthmüller, *Phys. Rev. B* **1996**, *54*, 11169.
- [47] G. Kresse, D. Joubert, *Phys. Rev. B* **1999**, *59*, 1758.
- [48] G. Kresse, J. Hafner, *Phys Rev B* **1993**, *47*, 558.
- [49] Y. Zhang, W. Yang, *Phys. Rev. Lett.* **1998**, *80*, 890.
- [50] T.-M. Guo, F.-F. Gao, Z.-G. Li, Y. Liu, M.-H. Yu, W. Li, *APL Mater.* **2020**, *8*, 101106.
- [51] K. Li, L.-Y. Dong, H.-X. Xu, Y. Qin, Z.-G. Li, M. Azeem, W. Li, X.-H. Bu, *Mater. Chem. Front.* **2019**, *3*, 1678.
- [52] M. K. Kohji Tashiro, H. Tadokoro, E. Fukadal, *Macromolecules* **1980**, *13*, 691.
- [53] H. Wang, H. Liu, Z. Zhang, Z. Liu, Z. Lv, T. Li, W. Ju, H. Li, X. Cai, H. Han, *npj Comput. Mater.* **2019**, *5*, 17.
- [54] F. Wang, Z. Dai, Y. Gu, X. Cheng, Y. Jiang, F. Ouyang, J. Xu, X. Xu, *RSC Adv.* **2018**, *8*, 16991.